Supporting Information

A synergetic strategy for advanced electrode with Fe_3O_4 embedded in 3D N-doped porous graphene framework and strong adhesive binder for ultralong cycle lifespan Lithium-/Potassium-Ion batteries

Ying Liu[a†], Donglin He[a†], Qiwei Tan[a], Qi Wan[b], Kun Han[a], Zhiwei Liu[a], Ping Li[a*], Fuqiang An[a] and Xuanhui Qu[a*]

[a] Beijing Advanced Innovation Center for Materials Genome Engineering, Institute for Advanced Materials and Technology, University of Science and Technology Beijing, Beijing 100083, China

[b] School of Materials Science and Engineering, Southwest University of Science and Technology, Mianyang 621010, China.

Email: ustbliping@126.com (P. L.); quxh@ustb.edu.cn (Prof. Xuanhui Qu)

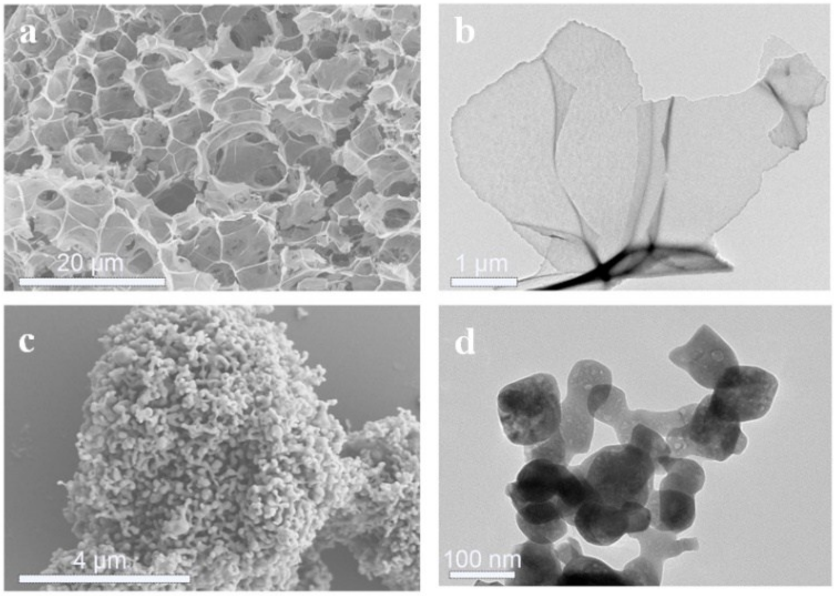

Fig. S1 SEM image of (a) pure 3DNPGF and (c) Fe_3O_4. TEM image of (b) pure 3DNPGF and (d) Fe_3O_4.

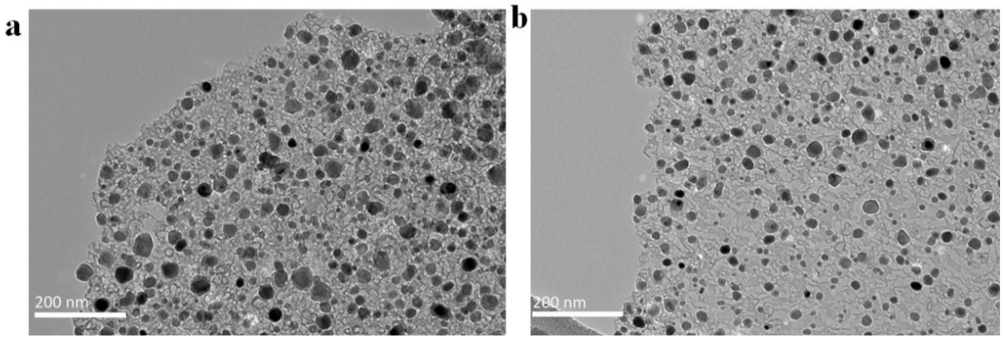

Fig. S2 TEM images of the Fe_3O_4/3DNPGF.

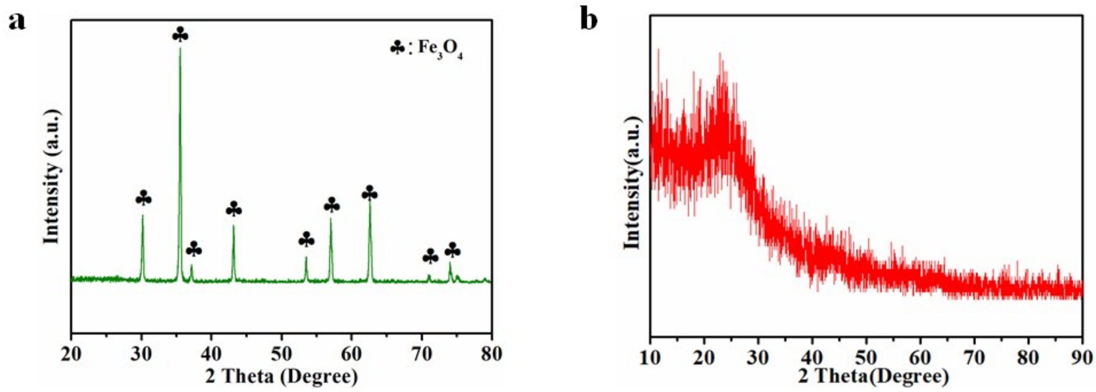

Fig. S3 XRD profile of (a) Fe_3O_4, and (b) pure 3DNPGF.

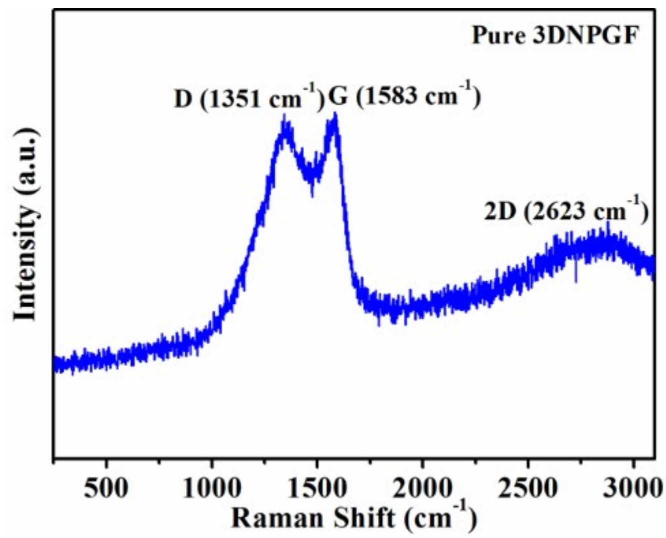

Fig. S4 Raman spectrum of pure 3DNPGF.

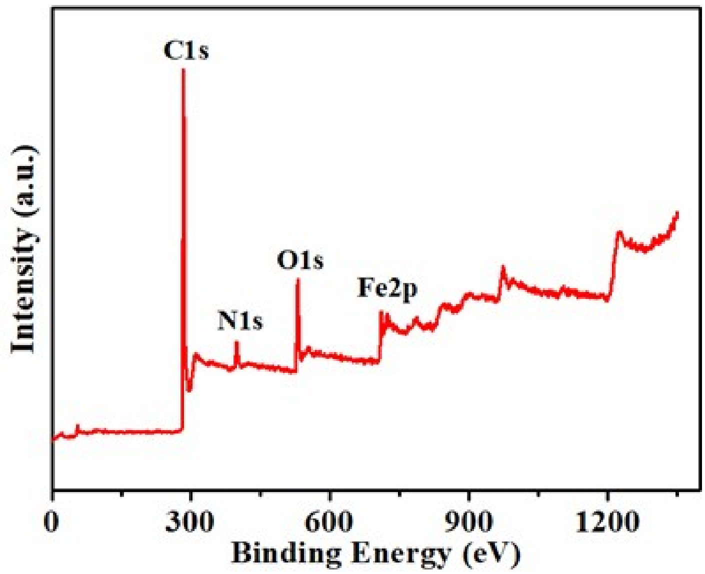

Fig. S5 XPS full survey profile of Fe_3O_4/3DNPGF.

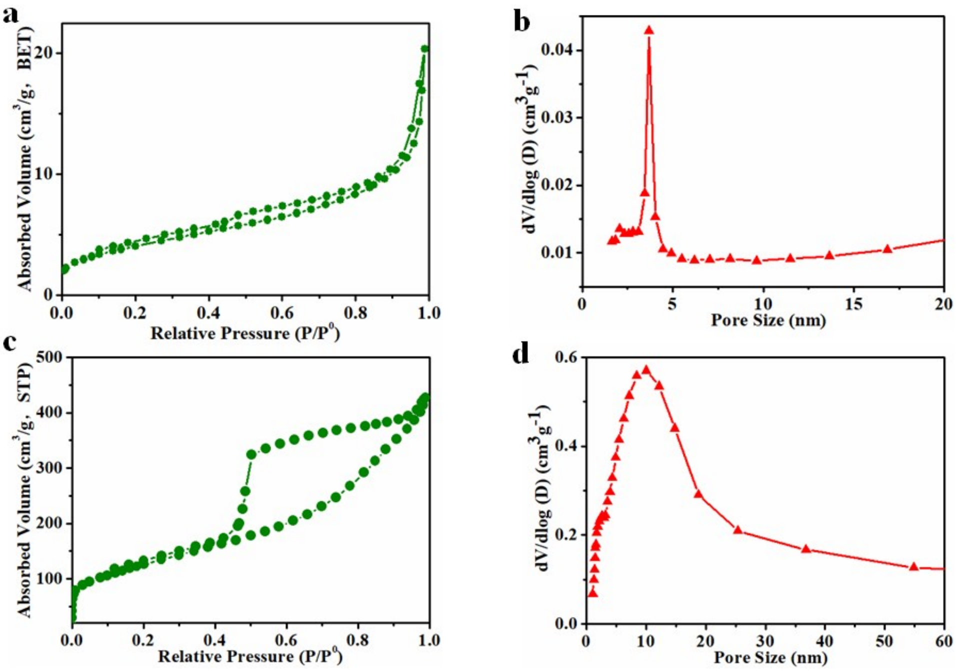

Fig. S6 Nitrogen adsorption-desorption isotherms and pore size distributions of (a, b) Fe_3O_4, and (c, d) pure 3DNPGF.

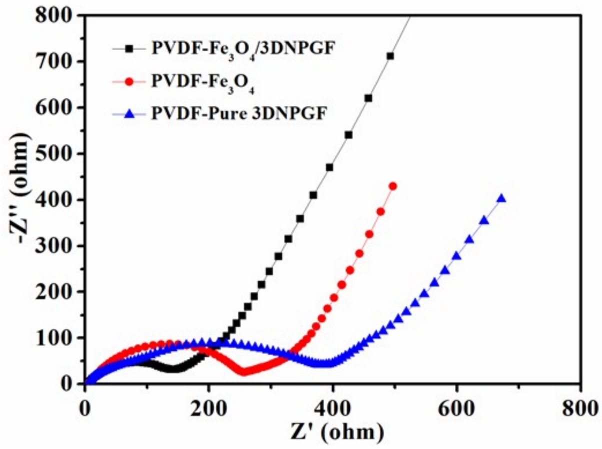

Fig. S7 EIS of the PVDF-Fe_3O_4/3DNPGF, PVDF-Fe3O4, and PVDF-pure 3DNPGF after 100 cycles in LIBs.

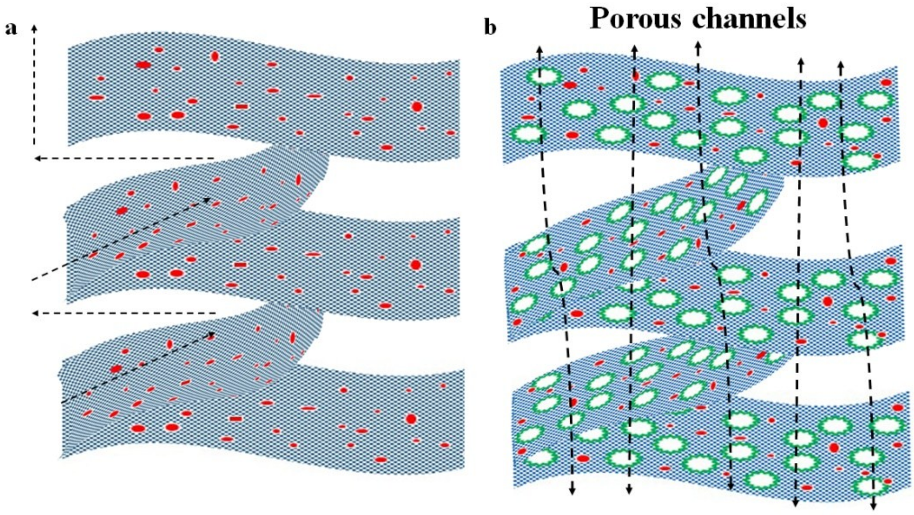

Fig. S8 The comparation of **a** nonporous, and **b** porous Fe_3O_4/3D graphene framework.

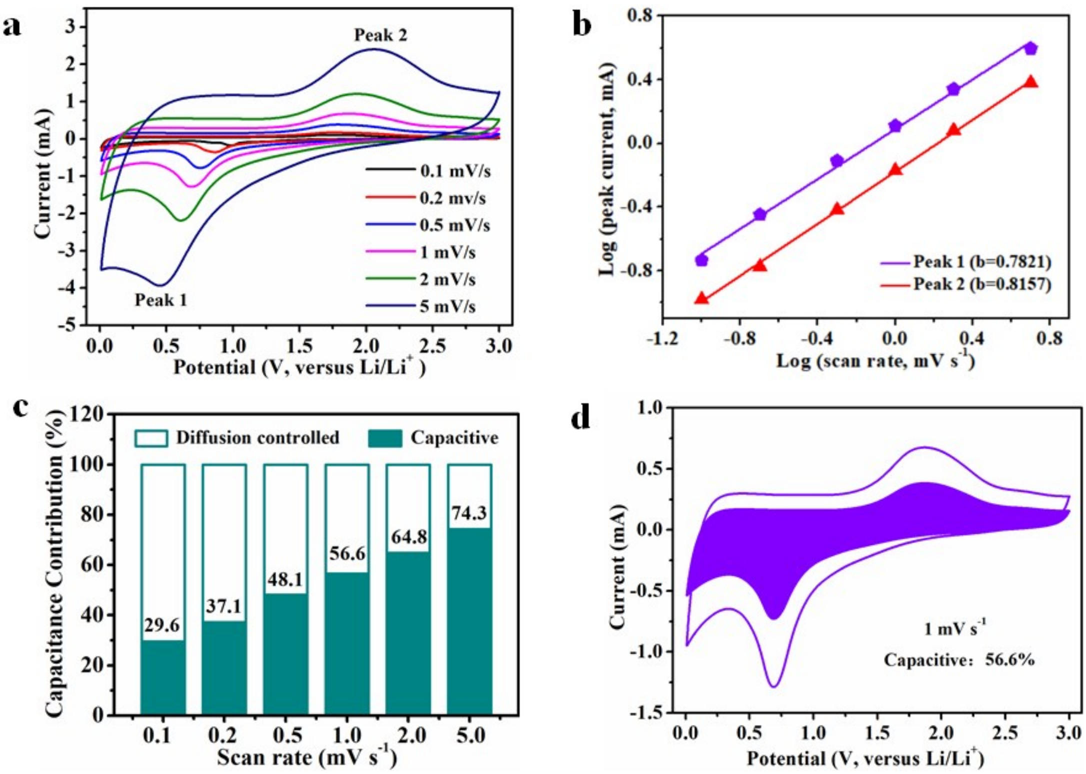

Fig. S9 The analysis of capacitive behavior for the Fe_3O_4/3DNPGF in LIBs. (a) CV profiles of the Fe_3O_4/3DNPGF at different scan rates (0.1~5.0 mV s^{-1}) between 0.01 to 3.0 V (vs Li^+/Li). (b) Determination of the b-value using the relationship between peak current and sweep rate. (c) Contribution ratio of the capacitive and diffusion-controlled charge versus scan rate, and (d) Purple curve shows the CV curve of the Fe_3O_4/3DNPGF and the shaded region indicates the capacitive contribution, measured at 1 mV s^{-1}.

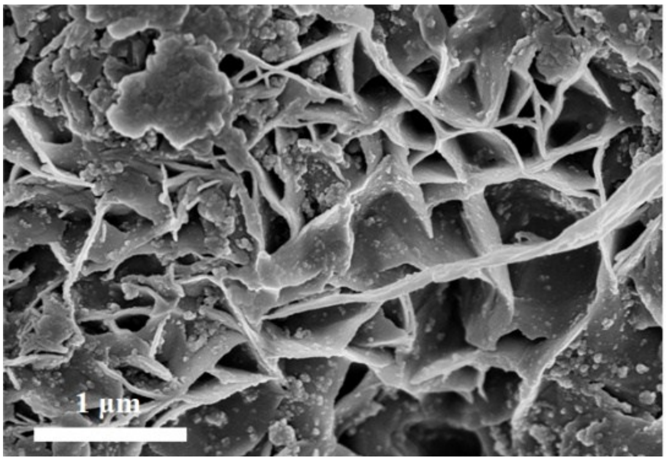

Fig. S10 SEM image of the PAA-Fe_3O_4/3DNPGF electrode after cycling in LIBs.

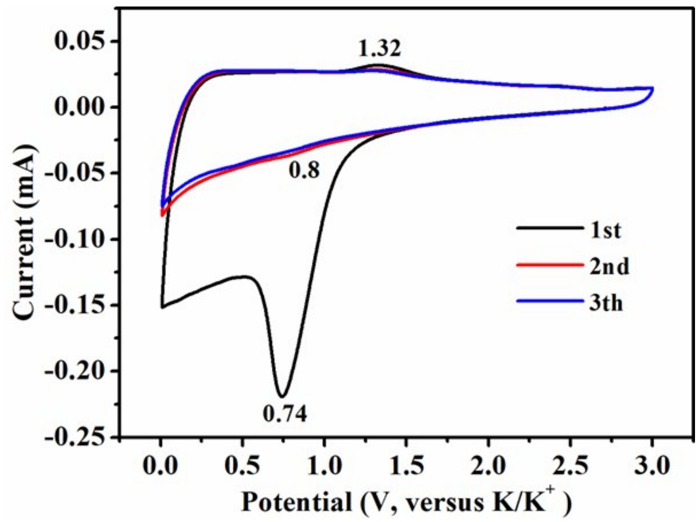

Fig. S11 Cyclic voltammetry curves of Fe_3O_4/3DNPGF in the potential range of 0.01 to 3.0 V (vs. K/K^+) at a scan rate of 0.1 mV s^{-1}.

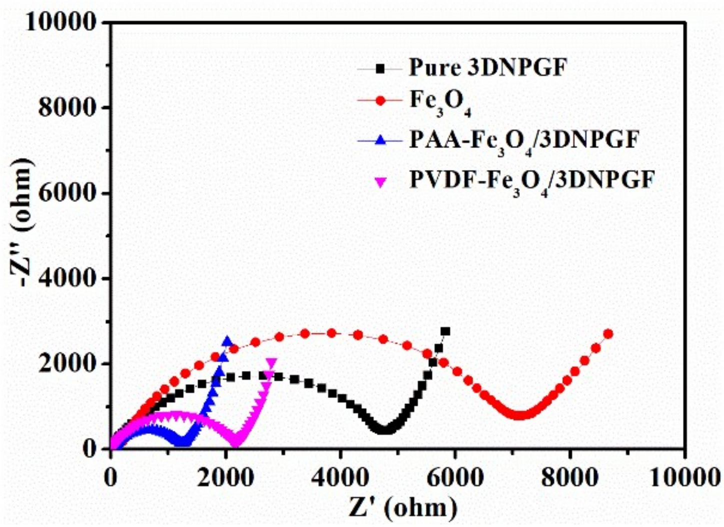

Fig. S12 Nyquist plots of EIS for the PAA-Fe_3O_4/3DNPGF, PVDF-Fe_3O_4/3DNPGF, Fe_3O_4, and pure 3DNPGF after 100 cycles in KIBs.

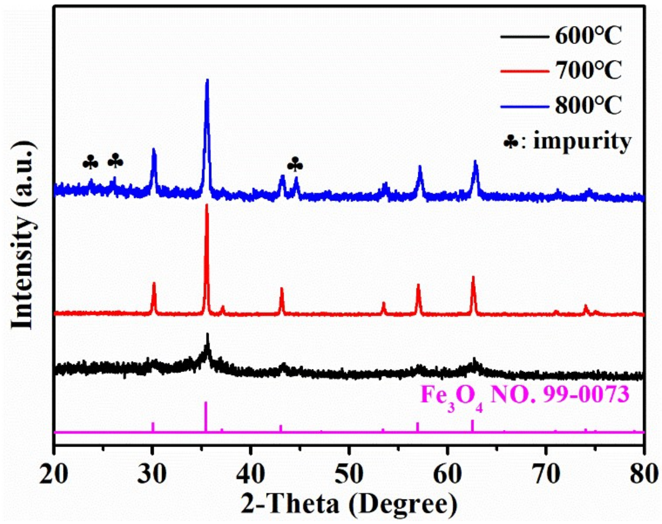

Fig. S13 XRD profile of Fe_3O_4/3DNPGF annealed at 600, 700, and 800 ℃.

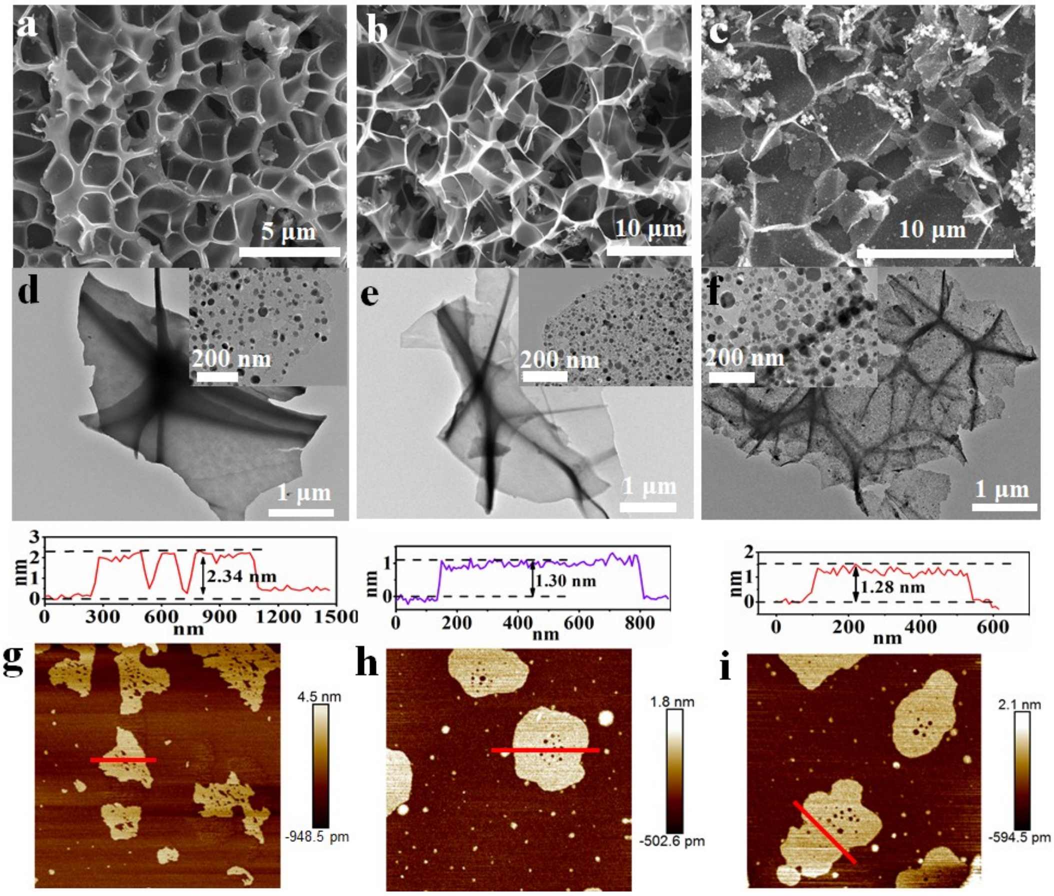

Fig. S14 (a-c) SEM images. (d-f) TEM images. (g-i) AFM images of Fe_3O_4/3DNPGF annealed at 600, 700, and 800 ℃, respectively.

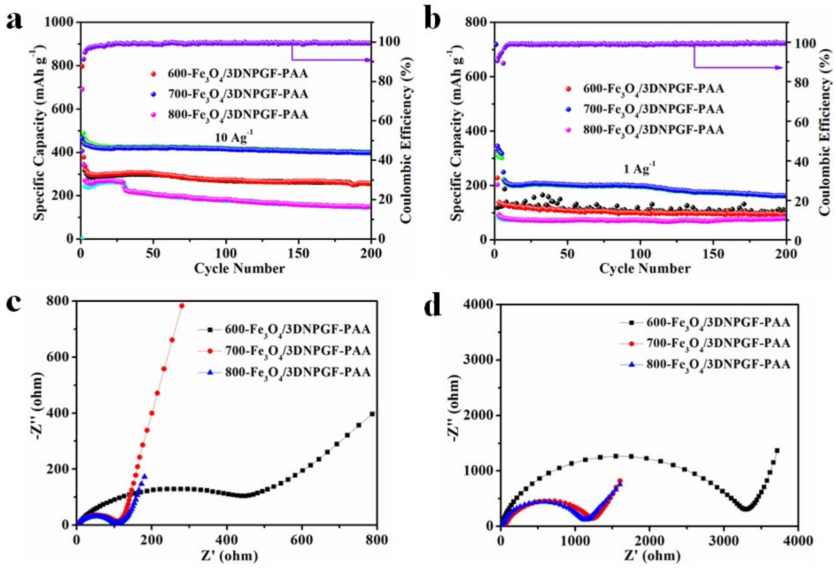

Fig. S15 Lithium/potassium storage properties of the PAA-Fe_3O_4/3DNPGF annealed at 600, 700, and 800 ℃. (a, c) Cycling performance and Nyquist plots of EIS at 10 A g^{-1} in LIBs. (b, d) Cycling performance and Nyquist plots of EIS at 1 A g^{-1} in KIBs.

The phase purity of the 600-Fe_3O_4/3DNPGF and 800-Fe_3O_4/3DNPGF samples are comparatively presented in Fig.S13, on which Fe_3O_4 (JCPDS: 99-0073) is identified as the major phase. However, the 600-Fe_3O_4/3DNPGF demonstrates lower crystallinity compared to the Fe_3O_4/3DNPGF (annealed at 700 ℃), whereas a few impurity peaks are observed on the XRD profile of the 800-Fe_3O_4/3DNPGF sample.

Fig. S14 compares the nanostructures of the 600-Fe_3O_4/3DNPGF, Fe_3O_4/3DNPGF, 800-Fe_3O_4/3DNPGF. Particularly, the 600-Fe_3O_4/3DNPGF are featured with thicker graphene nanosheets compared to that of the Fe_3O_4/3DNPGF and 800-Fe_3O_4/3DNPGF under the TEM observation, as further confirmed by AFM results (Fig. S14g-i). The thicker graphene nanosheets would result in reduced active surface area, and hinder ion transportation to some extent, [1] thus deteriorating electrochemical performance of the material. Besides, when annealed at 800 ℃, the severe particle aggregation effect at higher temperature results in the production of larger Fe_3O_4 nanoparticles decorated on the 3DNPGF matrix, as displayed in Fig. S14f. The larger Fe_3O_4 particles possess weaker tolerance toward the mechanical stress arising from the serious volume fluctuations upon cycling, leading to inferior structural robustness and poor battery performance. [2]

The lithium/potassium storage properties of the PAA-Fe_3O_4/3DNPGF at 600, 700, and 800 ℃ were further investigated by EIS and galvanostatic charge-discharge tests (Fig. S15). It is demonstrated that the Fe_3O_4/3DNPGF exhibits better battery performance in both LIBs and KIBs than the 600-Fe_3O_4/3DNPGF and 800-Fe_3O_4/3DNPGF electrodes. Benefiting from the structure-induced merits, the Fe_3O_4/3DNPGF at 700 ℃ retains a superb reversible capacity of 400.5 mAh g^{-1} after 200 cycles at 10 A g^{-1} for lithium storage. As for KIBs, the Fe_3O_4/3DNPGF electrode could still maintain a high capacity of 161.6 mAh g^{-1} after 200 cycles at 1 A g^{-1} and display a tiny capacity drop rate of 0.035% per cycle. Moreover, the EIS profiles reveal that the Fe_3O_4/3DNPGF electrode displays the lowest charge transfer resistance compared to the 600-Fe_3O_4/3DNPGF and 800-Fe_3O_4/3DNPGF electrodes (Fig. S15 c and d), implying the superior electrochemical kinetics of the Fe_3O_4/3DNPGF.

Table S1 An accurate Fe_3O_4 nanoparticles distribution in Fe_3O_4/3DNPGF

S[a] (nm)	P[b] (%)
5.0-9.3	12.90
9.3-13.6	21.77
13.6-17.9	20.16
17.9-22.2	15.32
22.2-26.5	12.90
26.5-30.8	8.06
30.8-35.1	4.03
35.1-39.4	1.61
39.4-43.7	2.42
43.7-48.0	0.81

[a] Particle size of the Fe_3O_4/3DNPGF

[b] Proportion of the Fe_3O_4 nanoparticles

Table S2 The ICP of Fe_3O_4/3DNPGF

Element	Content (wt%)
Fe	55.5
C	33.4
O	9.72
N	1.05

Table S3 The content of the N species in Fe_3O_4/3DNPGF

N species	Content (%)
Graphitic N	40.8
Pyrrolic N	37.1
Pyridinic N	22.1

Table S4 Pore structure of Fe_3O_4/NPGF, Fe_3O_4 and pure 3DNPGF

Sample	S_{BET}[a] (m^2 g^{-1})	$D_{average}$[b] (nm)	V_{Total}[c] (cm^3 g^{-1})	$V_{Mesoporou}$[d] (cm^3 g^{-1})	$P_{Mesoporou}$[e]
Fe_3O_4/3DNPGF	160.27	5.3508	0.210710	0.201941	95.84%
Pure 3DNPGF	446.6	5.8723	0.660622	0.620937	94%
Fe_3O_4	14.91	7.4398	0.031446	0.030066	95.6%

[a] Specific surface area calculated to BET (Brunauer-Emmett-Teller) method.

[b] Adsorption average pore diameter.

[c] Total pore volume.

[d] Mesopores volume.

[e] Percentage of mesopores.

Table S5 Recent progress on electrochemical performance of anodes for LIBs and KIBs

	Materials description	Cycling data [a)]	Capacity retention	Rate capability [b)]	Ref
LIBs	**Fe_3O_4/3DNPGF**	**990/100th/0.2**	**98.5%**	**168/15**	**This work**
		377.1/5000th/10	**81.4%**		
	Graphene-wrapped Fe_3O_4-graphene nanoribbons (G-Fe_3O_4-GNRs)	708/300th/0.4	88.5%	~525/1	3
	Mesoporous Fe_3O_4 nanospheres and graphene composites (Fe_3O_4-Ns/G)	~445/600th/2		440/2	4
	Fe_3O_4/N-doped graphene nanocomposites	929/70th/0.1	84.5%	491/4	5
	Graphene-encapsulated hollow Fe_3O_4 nanoparticle (G-HM)	900/50th/0.1	92%	580/0.8	6
	Graphene-Fe_3O_4@carbon composite (G-Fe_3O_4@C)	860/100th/0.1	90%	~460/2	7
	Fe_3O_4 cluster microspheres/graphene aerogels composite (Fe_3O_4/GAs)	650/500th/1	89.9%	603.5/2	8
	Fe_3O_4@graphene aerogel (Fe_3O_4@GA)	941.5/100th/0.1	57.8%	223.9/2	9
KIBs	**Fe_3O_4/3DNPGF**	**154.6/500th/1**	**76.4%**	**97.2/2**	**This work**
	Nanoporous Sb (NP-Sb)	318/50th/0.1	62.35%	265/0.5	10
	$MoSe_2$/N-doped Carbon ($MoSe_2$/N-C)	258.02/300th/0.1		196/1	11
	Red phosphorus@carbon nanosheet (red P@CN)	665/40th/0.1		323.7/2	12
	Graphitic carbon nanocage	195/100th/0.2C (1C=0.279)		175/35C	13
	N-doped porous Carbon	342.8/500th/0.1	90.9%	185/10	14

	Yolk-shell FeS_2@C	162/1000th/1		203/10	[15]
	$Co_3[Co(CN)_6]_2$	282/200th/0.5	82%	221/1	[16]
	CoSe2 threaded by N-doped carbon nanotubes	253/100th/0.2	~85.3%	173/2	[17]

[a)] The cycling data are summarized as capacity/corresponding cycle number/corresponding current density. The unit of capacity and current density is mAh g^{-1} and mA g^{-1}, respectively.

[b)] The rate capability is summarized as capacity/corresponding current density. The unit of capacity and current density is mAh g^{-1} and A g^{-1}, respectively.

References

1. Y. Jiang, Z.-J. Jiang, L. Yang, S. Cheng and M. Liu, *J. Mater. Chem. A*, 2015, **3**, 11847-11856.
2. G. Chen, M. Zhou, J. Catanach, T. Liaw, L. Fei, S. Deng and H. Luo, *Nano Energy*, 2014, **8**, 126-132.
3. L. Li, A. Kovalchuk, H. Fei, Z. Peng, Y. Li, N. D. Kim, C. Xiang, Y. Yang, G. Ruan and J. M. Tour, *Adv. Energy Mater.*, 2015, **5**.
4. Y. Dong, K. C. Yung, R. Ma, X. Yang, Y.-S. Chui, J.-M. Lee and J. A. Zapien, *Carbon*, 2015, **86**, 310-317.
5. J. Jiao, W. Qiu, J. Tang, L. Chen and L. Jing, *Nano Research*, 2016, **9**, 1256-1266.
6. D. Chen, G. Ji, Y. Ma, J. Y. Lee and J. Lu, *ACS Appl. Mater. Interfaces*, 2011, **3**, 3078-3083.
7. L. Zhao, M. Gao, W. Yue, Y. Jiang, Y. Wang, Y. Ren and F. Hu, *ACS Appl. Mater. Interfaces*, 2015, **7**, 9709-9715.
8. S. Zhou, Y. Zhou, W. Jiang, H. Guo, Z. Wang and X. Li, *Appl. Surf. Sci.*, 2018, **439**, 927-933.
9. Y. Suo, Q.-Q. Zhao, J.-K. Meng, J. Li, X.-C. Zheng, X.-X. Guan, Y.-S. Liu and J.-M. Zhang, *Mater. Lett.*, 2016, **174**, 36-39.
10. Y. An, Y. Tian, L. Ci, S. Xiong, J. Feng and Y. Qian, *Acs Nano*, 2018, **12**, 12932-12940.
11. J. Ge, L. Fan, J. Wang, Q. Zhang, Z. Liu, E. Zhang, Q. Liu, X. Yu and B. Lu, *Adv. Energy Mater.*, 2018, **8**, 1801477.
12. P. Xiong, P. Bai, S. Tu, M. Cheng, J. Zhang, J. Sun and Y. Xu, *Small*, 2018, **14**, 1802140.
13. B. Cao, Q. Zhang, H. Liu, B. Xu, S. Zhang, T. Zhou, J. Mao, W. K. Pang, Z. Guo, A. Li, J. Zhou, X. Chen and H. Song, *Adv. Energy Mater.*, 2018, **8**, 1801149.
14. D. Li, X. Ren, Q. Ai, Q. Sun, L. Zhu, Y. Liu, Z. Liang, R. Peng, P. Si, J. Lou, J. Feng and L. Ci, *Adv. Energy Mater.*, 2018, **8**, 1802386.
15. Y. Zhao, J. Zhu, S. J. H. Ong, Q. Yao, X. Shi, K. Hou, Z. J. Xu and L. Guan, *Adv. Energy Mater.*, 2018, **8**, 1802565.
16. L. Deng, Z. Yang, L. Tan, L. Zeng, Y. Zhu and L. Guo, *Adv. Mater.*, 2018, **30**, 1802510.
17. Q. Yu, B. Jiang, J. Hu, C.-Y. Lao, Y. Gao, P. Li, Z. Liu, G. Suo, D. He, W. Wang and G. Yin, *Advanced Science*, 2018, **5**, 1800782.